StereoBaseLine: a flexible system for photogrammetric data acquisition in a linear configuration

Mehdi Daakir[1], Aubin Bettiol[2]

[1]Univ. Gustave Eiffel, IGN, ENSG, LASTIG lab, 77420 Champs-sur-Marne, France
[2] EDF DTG-TOPO, 12 rue St. Sidoine, 69003 Lyon, France
(mehdi.daakir@ign.fr, aubin.bettiol@edf.fr)

Commission I

Keywords: calibration, integrated sensor orientation, GNSS, rigid block constraint, corridor mapping, open-source

Abstract

This paper evaluates the georeferencing accuracy of the "StereoBaseLine" (SBL) system, a lightweight, low-cost mapping solution composed of two consumer-grade cameras and two GNSS sensors, designed and assembled in-house. In its standard operation, the SBL captures two synchronized images and two GNSS positions at each trigger event. The system is primarily intended for linear acquisition configurations. Given this specific geometry, the use of pre-calibrated parameters is employed to constrain the photogrammetric Bundle Block Adjustment (BBA), helping to prevent drift over long distances. This is achieved through a combination of GNSS observations and Rigid Block Constraint (RBC). To assess the effectiveness of these constraints in improving georeferencing accuracy without relying on Ground Control Points (GCPs), we present results from both a dedicated calibration and evaluation dataset, followed by a large-scale case study. The performances obtained with the system are presented, analyzed and discussed.

1. Introduction

Multi-sensor systems combining cameras, GNSS, and inertial measurement units (IMU) are increasingly employed in mobile mapping applications, in aerial, terrestrial, and indoor environments (Puente et al., 2013, Elhashash et al., 2022). Although highly effective in aerial context where reliable GNSS signals ensure accurate georeferencing, these systems face challenges in urban areas due to obstructions and multi-path effect (Jeong et al., 2019). Multi-view imaging platforms enhance mapping by synchronizing multiple cameras, providing broad coverage and dense stereoscopic imagery (Cavegn and Haala, 2016). Direct Georeferencing (DG) and Integrated Sensor Orientation (InSO) offer strong initial estimates and constraints for Bundle Block Adjustment (BBA) when robust pre-calibration (Skaloud, 2006) is performed. These constraints help mitigate systematic errors such as the "bowl effect" (James and Robson, 2014), which is common in corridor mapping with elongated trajectories sometimes without loop closures. Although Ground Control Points (GCPs) are typically used to correct such drift, their use is often impractical in large-scale or inaccessible areas. To overcome these limitations, constrained BBA strategies leverage multi-camera setups and navigation sensor coupling to exploit relative parameters between systems. Empirical studies have shown that such approaches by introducing a rigidity block constraint while dealing with multi-camera systems can significantly improve object-space accuracy over traditional BBA (Maset et al., 2021). Similar benefits have been demonstrated in GNSS constrained environments, particularly with UAV imagery over long linear corridors captured by consumer-grade cameras (Huang et al., 2021).

In this context, we examine the georeferencing performance of the "StereoBaseLine" (SBL) system, a lightweight, custom-built mapping platform designed specifically for long linear scenes without relying on GCPs. The SBL integrates two consumer-grade cameras and a dual GNSS setup to capture synchronized imagery and positioning data at each acquisition step. This study evaluates how effectively the system's inherent design constraints reduce drift and improve georeferencing accuracy, first in controlled calibration and evaluation environments, and then on a complex, large-scale real-world use-case.

2. Hardware system

In this section, we present the hardware components constituting the acquisition system. We also evaluate the synchronization quality by testing two triggering modes, direct and external, as well as different acquisition frequencies, intervalometer and on-demand triggering.

2.1 Sensors

The SBL system is composed of two consumer-grade cameras, each linked to an individual GNSS receiver via the hot shoe interface. The entire setup is assembled using custom, in-house designed mechanical components manufactured through resin 3D printing to build precise and smooth components, ensuring a rigid and stable configuration. A synchronization remote controller is connected to the cameras, allowing for simultaneous image capture. The "exact" moment of shutter release is recorded by the GNSS receivers through the hot shoe trigger, providing precise time-stamping and alignment of all data to a unified reference timescale. Figure 1 shows the SBL components while the main technical specifications of the sensors integrated into the SBL system are summarized in Table 1.

2.2 Time synchronization

The reliability of the rigid structure of the SBL system relies also on the synchronization of all its sensors. To ensure this synchronization, two different hardware assemblies were tested, each designed to assess the most convenient and effective operational use of the system. Desynchronization between the

Figure 1. (a): `GEOSTIX-X5 GNSS` receiver ; (b): hot shoe synchronization interface; (c): `SONY ILCE-A6400` camera; (d): `SONY SEL16F28` lens; (e): mechanical interface design.

`GEOSTIX-X5 GNSS` receiver
Satellite Constellations: `G/R/E/B`
Frequencies: `L1/L2/L5`
σ_{RTK} Horizontal (hor.): 0.6 cm + 0.5 ppm
σ_{RTK} Vertical (vert.): 1.0 cm + 1.0 ppm
`SONY ILCE-A6400` Camera
Sensor Format: 23.5 mm x 15.6 mm
Resolution: 6000 px x 4000 px
Pixel Size: 3.9 µm x 3.9 µm
`SONY SEL16F28` Lens
Focal Length (fixed): 16 mm
Field of View: 73° x 28°

Table 1. `SBL` sensors technical specifications

components is evaluated by comparing the `GNSS` time-stamps recorded by the two receivers.

In the first setup, the cameras are connected using a `SONY VMC MM2` cable. This cable has a fixed directionality that enables the slave camera to be triggered automatically when the master camera is triggered. Although this solution is straightforward and requires only a single cable, it is not ideal for remote operations, as it necessitates manually pressing the shutter button on the master camera. To address this limitation, a second configuration was implemented using an external trigger system. In this setup, a `NEEWER RST7001` remote controller is used to send the trigger signal simultaneously to both cameras via a jack cable splitter. While this arrangement is slightly more complex, it allows for remote operation of the `SBL`, either manually or automatically using the remote controller in intervalometer mode. Both configurations are illustrated in Figure 2.

The second configuration was ultimately adopted due to its practicality, enabling the system to operate without any physical interaction with the cameras. The next step is to evaluate the synchronization quality of the system under this setup. A key aspect of this assessment is ensuring that the output delay introduced by the jack splitter cable remains negligible. To verify this, the two trigger signals were measured using an oscilloscope. Figure 3 shows the resulting waveforms. A voltage offset of 0.2 V was applied to one of the signals to aid in visual comparison. The duration of the signal transition is approximately 0.8 µs, and the signals overlap within fractions of a division, each division representing a duration of 250 ns. These observations indicate that the delay between the two signals at the output of the splitter is negligible, confirming effective synchronization at this stage.

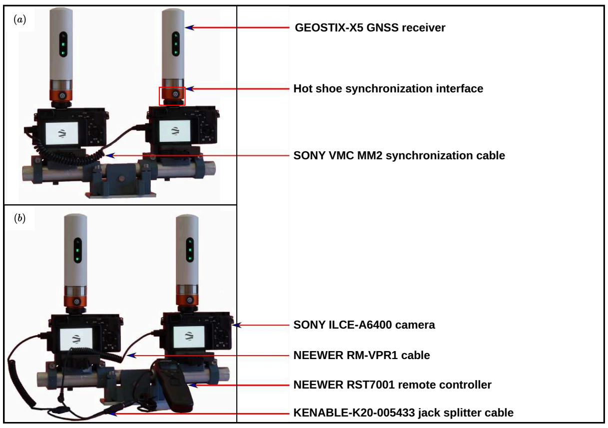

Figure 2. `SBL` triggering configurations: (a) direct synchronization via cable connection, (b) external remote triggering system.

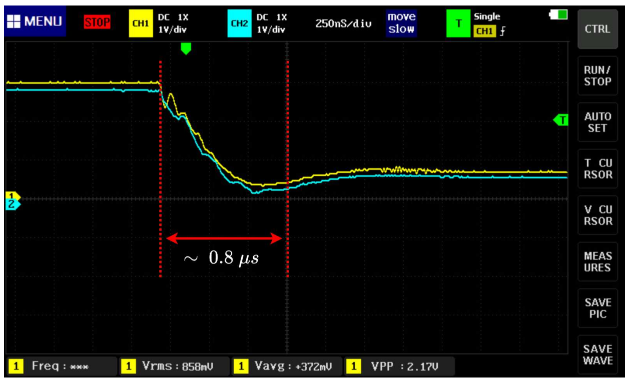

Figure 3. Measurement of the signal delay at the output of the jack splitter connecting the external trigger remote controller to both cameras.

However, several additional factors must be considered: (i) the electronic delay between the moment the trigger command is issued to the camera and the moment the flash signal is sent via the hot shoe interface. This delay, known as the flash trigger delay, is typically undocumented and difficult to measure, as manufacturers rarely provide specifications for it; (ii) the transmission delay of the flash signal from the hot shoe interface to the `GNSS` receiver is negligible, on the order of a few nanoseconds; (iii) the time-stamping of the event by the `GNSS` receiver: the `GEOSTIX-X5` devices used in this setup are equipped with the `Septentrio Mosaic-X5 GNSS` module, which supports external event time-stamping through electrical level transitions on its `EventX` port. According to the manufacturer, the typical time-stamping error is within 20 ns (Septentrio, 2023).

Considering these elements, the primary source of synchronization error can be attributed to the flash trigger delay. It is also important to note that this delay is influenced by the camera settings. For consistent performance, the cameras are operated in full Manual (M) mode with manual focus. Measurements were conducted under two operational modes of the external trigger system: (i) intervalometer mode, with trigger intervals of 2 s, 3 s, and 5 s, and (ii) on-demand manual trigger mode. Figure 4 presents the measured desynchronization values, derived from time-stamp differences recorded by the two GNSS receivers across various tests.

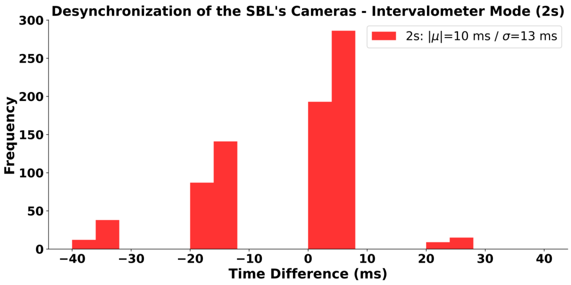

(a)

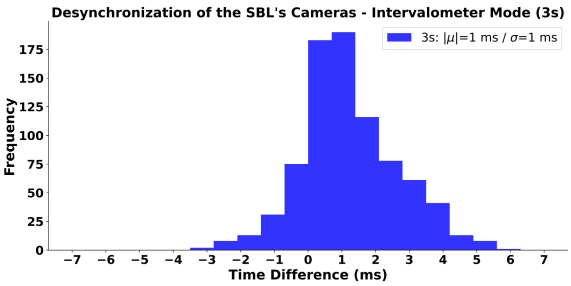

(b)

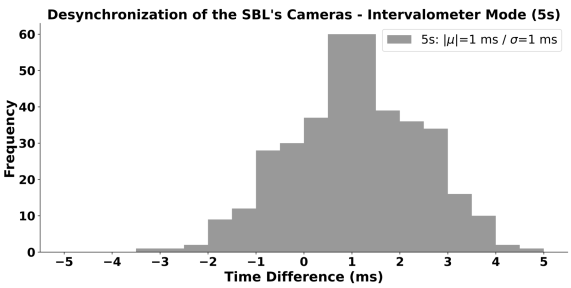

(c)

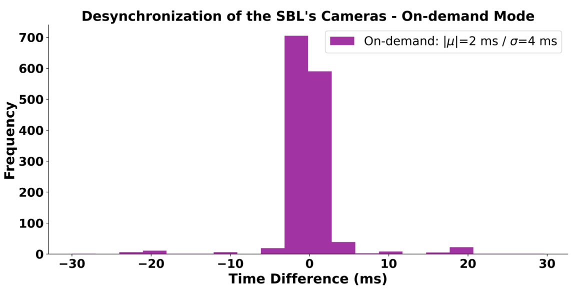

(d)

Figure 4. Histogram of the desynchronization values between the two cameras: (a), (b), and (c) correspond to intervalometer mode with 2 s, 3 s, and 5 s intervals respectively; (d) corresponds to on-demand triggering mode.

In intervalometer mode, acquisition frequencies of 3 s and 5 s result in average absolute desynchronization values of 1 ms, with a standard deviation also of $\pm 1\,\mathrm{ms}$. However, the highest acquisition frequency offered by the external controller (2 s) does not allow the system to function reliably. The measured delays appear to cluster around four values spaced by $20\,\mathrm{ms}$.

In the on-demand triggering mode, which is the preferred operational mode, as we can operate the system under the desired acquisition frequency, we also observe a few instances where the desynchronization is significantly high, up to $20\,\mathrm{ms}$. Given that the primary use case of the SBL system is terrestrial close-range photogrammetric surveying where the typical operating speed is relatively low: e.g., walking velocity of approximately $1.4\,\mathrm{m/s}$ and a desynchronization error of $2\,\mathrm{ms}$ results in a spatial offset of $2.8\,\mathrm{mm}$. To minimize the influence of such timing discrepancies, calibration acquisitions are performed with the system in a static position, while all operational acquisitions are carried out in stop-and-go mode.

3. System calibration & evaluation

This section outlines the calibration procedure adopted for our system and evaluates its expected performance in a linear acquisition setup under controlled conditions.

3.1 System Calibration

The first essential step after the mechanical assembly of the system is its calibration. Several components require calibration in this configuration, as detailed below:

- $(\zeta_{\mathtt{C1}}, \zeta_{\mathtt{C2}})$: calibration of the interior orientation parameters of both cameras
- $(\vec{\mathtt{L}}_{(\mathtt{C1},\mathtt{G1})}, \vec{\mathtt{L}}_{(\mathtt{C2},\mathtt{G2})})$: calibration of the lever-arm vectors between the optical centers of the cameras and the phase centers of their respective GNSS receivers
- $\vec{\mathtt{L}}_{(\mathtt{C1},\mathtt{C2})}$: calibration of the lever-arm vector between the optical centers of the two cameras
- $\mathtt{R}_{(\mathtt{C2}\rightarrow\mathtt{C1})}$: calibration of the boresight rotation matrix from camera C2 to camera C1 (by convention, camera C1 is defined as the reference or master camera, and its position and orientation are the identity matrix within the block.)

Figure 6 illustrates the geometry of the SBL system.

A dedicated calibration polygon was established for this purpose. The goal is to create a textured scene containing multiple photogrammetric targets, Ground Control Points (GCPs and Check Points (CPs), positioned at varying depths. These targets are surveyed using optical topometric instruments to ensure accurate 3D reference coordinates. Since the SBL system incorporates GNSS receivers, the target coordinates must also be expressed within a global geodetic reference frame. To facilitate precise image-based measurements, circular automatically detected coded targets, slightly adapted for compatibility with both topometric and imaging systems (Muller et al., 2024) were placed throughout the scene . Table 2 summarizes the main characteristics of the calibration scene, while Figure 5 illustrates the photogrammetric acquisition geometry.

The processing of angular and distance observations to estimate the coordinates of the photogrammetric targets was performed using the free open-source topometric adjustment software Comp3D (IGN, 2024). The calibration dataset consists of two image acquisition sequences, with the SBL mounted on a photographic tripod to enable static captures (see Figure 7).

Polygon main characteristics
$N_{\texttt{Observations}}$: 1130
$N_{\texttt{Parameters}}$: 271
$N_{\texttt{GNSS}}$: 3
avg. duration observation: $\sim$20 h
avg. uncertainty on GNSS:
- hor. 4 mm
- vert. 9 mm
avg. rel. uncertainty on GCPs: 0.3 mm
avg. abs. uncertainty on GCPs:
- hor. 2 mm
- vert. 5 mm

Table 2. Key characteristics of the surveyed point network for system calibration.

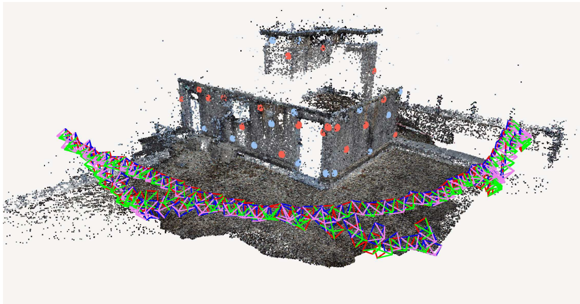

Figure 5. Acquisition geometry for system calibration: camera positions, 3D tie points (black), GCPs (red), and CPs (blue).

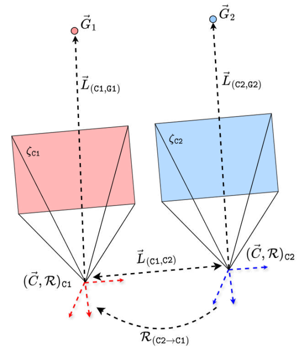

Figure 6. Illustration of the SBL geometry, highlighting the geometric parameters to be calibrated.

Figure 7. Rear view of the SBL system mounted on a photo tripod.

In the first sequence, the GNSS receivers were not mounted on the cameras, allowing the acquisition of stereo images with the SBL in various orientations without compromising the GNSS signal. The second sequence was conducted with the SBL in its final configuration, enabling simultaneous acquisition of GNSS and image data. Table 3 summarizes the key characteristics of the calibration dataset.

Calibration dataset
$N_{\texttt{Images}}$: 130
$N_{\texttt{GNSS}}$: 64
$N_{\texttt{GCPs}}$: 35
GNSS ambiguity fix rate: 100%
avg. uncertainty on GNSS:
- hor. 24 mm
- vert. 28 mm

Table 3. Main characteristics of the calibration dataset

The goal is to estimate the parameters listed in Section 3.1. For each camera the adopted camera model is a standard 12-degree-of-freedom model (Fraser, 1997), which includes: one parameter for focal length, two for the principal point, two for the distortion center, three for radial distortion coefficients, two for decentering distortion, and two for affine parameters. This estimation is performed through a constrained bundle block adjustment approach (Pierrot Deseilligny and Cléry, 2012), incorporating multiple types of observations: (i) image measurements of tie points, (ii) 2D–3D correspondences from GCPs, (iii) camera positions from GNSS receivers and (iv) rigid block constraint. The objective is to minimize a global cost function (Zhou et al., 2018) defined as follows:

$$\mathcal{E}_{\texttt{total}} = \mathcal{E}_{\texttt{img}} + \mathcal{E}_{\texttt{GNSS}} + \mathcal{E}_{\texttt{GCP}} + \mathcal{E}_{\texttt{RBC}} \tag{1}$$

where:

$$\mathcal{E}_{\texttt{img}} = \sum_{l=1}^{L}\sum_{m=1}^{M} \frac{\left\|\mathbf{p}_l^m - \zeta\left(\pi(\mathbf{R}_m(\mathbf{P}_l - \mathbf{C}_m))\right)\right\|^2}{\sigma_{img}^2} \tag{2}$$

$$\mathcal{E}_{\texttt{GNSS}} = \sum_{k=1}^{K}\sum_{z=1}^{Z} \frac{\left\|\mathbf{R}_k(\mathbf{C}_k - \mathbf{G}_k) - \boldsymbol{L}_z\right\|^2}{\sigma_{\texttt{GNSS}}^2} \tag{3}$$

$$\mathcal{E}_{\texttt{GCP}} = \sum_{n=1}^{N}\sum_{m=1}^{M} \frac{\left\|\mathbf{p}_n^m - \zeta\left(\pi(\mathbf{R}_m(\mathbf{P}_{\texttt{GCP},n} - \mathbf{C}_m))\right)\right\|^2}{\sigma_{img,\texttt{GCP}}^2} + \sum_{n=1}^{N} \frac{\left\|\mathbf{P}_n - \mathbf{P}_{\texttt{GCP},n}\right\|^2}{\sigma_{\texttt{GCP}}^2} \tag{4}$$

and:

- l, m, k, z, n are indexes of respectively: tie points, image, GNSS position; lever-arm group of images (C1-G1 or C2-G2 in this case), GCPs;
- $\mathbf{p}_l^m$, $\mathbf{p}_n^m$ are the 2D image coordinates of tie point l and GCP n in image m;
- $\mathbf{P}_l$, $\mathbf{P}_n$, $\mathbf{P}_{\texttt{GCP},n}$ are the 3D positions of tie point, estimated GCP by pseudo-intersection, and ground measured GCP;
- $(\mathbf{R}_m, \mathbf{C}_m)$ are the exterior parameters of image m;
- $\mathbf{C}_k$, $\mathbf{G}_k$ are the camera center and GNSS antenna phase center position associated to image k;
- $\boldsymbol{L}_z$ is the lever-arm offset for group z;
- π is the projection function, and ζ the camera interior model;
- $\sigma_{\texttt{img}}$, $\sigma_{\texttt{GNSS}}$, $\sigma_{img,\texttt{GCP}}$, $\sigma_{\texttt{GCP}}$ are the weights of corresponding observations;

To introduce the rigid block constraint, an additional term $\mathcal{E}_{\texttt{RBC}}$ is added to the global energy expression to penalize deviations from the rigidity hypothesis. In MicMac (Rupnik et al., 2017), different strategies are offered depending on the context:

- **Calibration mode**: the goal is to estimate unknown relative parameters between sub-cameras. Initial values can be computed by averaging the pose differences at each trigger index, along with a dispersion indicator giving a rigidity prior. In this context, the penalization term encourages the relative transformations to remain consistent across the block.

- **Attachment mode**: the objective is to constrain the solution to remain close to a known value, within a certain uncertainty. This is useful when prior calibration values are available. The corresponding penalization term enforces adherence to these reference values.

- **Temporal constraint mode**: this mode is designed for systems whose rigidity may evolve over time, for instance, due to mechanical deformation. It assumes that consecutive blocks are similar, but can drift gradually. The regularization term introduces smooth temporal transitions.

Each mode reflects a different prior assumption on the rigidity of the system, and the choice of a priori standard deviations allows adjusting the strength of the constraint. The expressions of the terms $\mathcal{E}_{\mathtt{RBC}}$ as functions of the modes are detailed in the `MicMac` documentation (Pierrot-Deseilligny et al., 2014).

To evaluate the quality of the calibration process, several metrics are considered: (i) residuals from the prediction of `CPs` (see Figure 8a), (ii) residuals from the estimation of `GNSS` lever-arms (see Figure 8b), and (iii) the variation in translation and rotation parameters between the two cameras, which reflects the stability of the cameras block (see Figure 8c). Table 4 provides a summary of the geometric parameters characterizing the system, along with their associated dispersion.

	$\vec{L}_{(\mathtt{C1,G1})}$	$\vec{L}_{(\mathtt{C2,G2})}$	$\vec{L}_{(\mathtt{C1,C2})}$	$R_{(\mathtt{C2}\to\mathtt{C1})}$
δx [mm]	19 ± 12	24 ± 12	200.1 ± 0.5	-
δy [mm]	-221 ± 16	-206 ± 10	1.0 ± 0.6	-
δz [mm]	-47 ± 19	-56 ± 10	0.2 ± 0.2	-
$\delta\omega$ [°]	-	-	-	0.12 ± 0.08
$\delta\phi$ [°]	-	-	-	0.64 ± 0.09
$\delta\kappa$ [°]	-	-	-	0.60 ± 0.03

Table 4. Geometric parameters characterizing the acquisition system.

The prediction on `CPs` yields an average `3D` error of 4 mm with an uncertainty of $\pm$ 1 mm, which is on the same order of magnitude as the average absolute uncertainty of the point network determined by topometric measurements. The lever-arms between the cameras and the `GNSS` receivers are determined with an error of 23 mm with an uncertainty of $\pm$17 mm for the pair `C1–G1`, and an error of 19 mm with an uncertainty of $\pm$7 mm for the pair `C2–G2`. The better performance of the `GNSS` receiver `G2` is due to its higher quality antenna.

As for the parameters linking the two camera block, the inter camera lever-arm is estimated with a bias of 0.4 mm and a dispersion of $\pm$0.5 mm. Finally, the boresight matrix between the two cameras is determined with angular uncertainties ranging from 0.03° to 0.09° depending on the axis.

3.2 System evaluation

To assess the performance of the `SBL` system, an independent evaluation scene was established. A linear acquisition was conducted over this scene, where several `CPs` were marked and measured using a geodetic-grade `Trimble R12 GNSS` receiver. Although this scene does not reflect the final use-case configuration (see Section 4), it provides an estimate of the system's "optimal performance" thanks to its well-textured environment and mostly open-sky conditions ensuring excellent `GNSS` signal reception. Moreover, its proximity to the calibration scene (see Figure 9a) ensures consistency in acquisition conditions. The acquisition geometry is shown in Figure 9b, and the main characteristics of the evaluation dataset are summarized in Table 5.

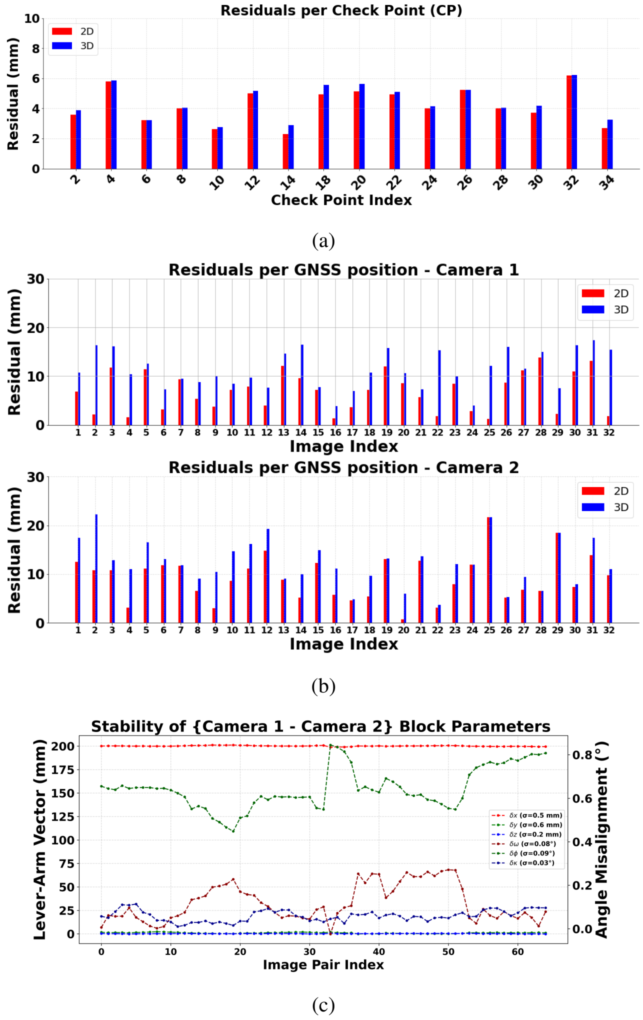

Figure 8. Assessment of calibration quality: (a) residuals on `CPs`, (b) residuals on `GNSS` positions, (c) stability of the cameras block parameters of the system.

Evaluation dataset
$N_{\mathtt{Images}}$: 246
Length of acquisition: $\sim$ 80 m
$N_{\mathtt{CPs}}$: 15
avg. uncertainty on `CPs`:
- hor. 6 mm
- vert. 10 mm
`GNSS` ambiguity fix rate: 100%
avg. uncertainty on `GNSS`:
- hor. 23 mm
- vert. 31 mm

Table 5. Main characteristics of the evaluation dataset

For this configuration, we adopt the same approach as used during the calibration step, with the only difference being that the previously estimated parameters are not considered as unknowns. This is particularly true for the `GNSS` lever-arms and rigid-block parameters, whose re-estimation is not accurate since the minimized energy function corresponds to Equation 1 without the $\mathcal{E}_{\mathtt{GCP}}$ term. To assess the performance of our system, residuals at `CPs` are evaluated. Figure 10 shows the results obtained.

The prediction on the `CPs` yields an average `3D` error of 22 mm with an uncertainty of $\pm$ 5 mm. Under optimal conditions, the `SBL` system provides a high level georeferencing performance

https://doi.org/10.5194/isprs-archives-XLVIII-1-W4-2025-29-2025 | © Author(s) 2025. CC BY 4.0 License.

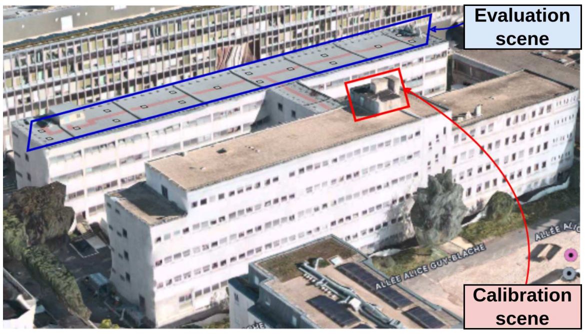

(a)

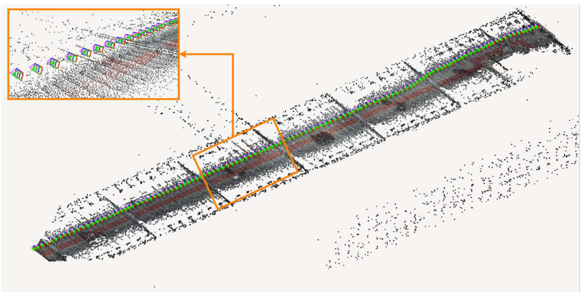

(b)

Figure 9. (a): Aerial view showing the calibration and evaluation scenes on the rooftop of the IGN (French Mapping Agency) building; (b): Acquisition geometry of the evaluation dataset.

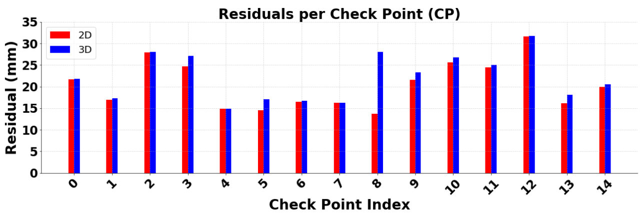

Figure 10. Residuals on CPs

that meets the accuracy requirements of many field measurement applications.

4. The Olympic bobsleigh track use-case

The Olympic bobsleigh track is located in the French Alps in the village of Aime-la-Plagne. Constructed between 1988 and 1990, the track hosted the bobsleigh and luge events during the 1992 Winter Olympic Games of Albertville. The track is 1830 m in length, featuring a winding path composed of 19 curves and an altitude difference of 124 m, resulting in an average slope of approximately 5.5% (Chazalet, 1991).

Data collection of our experimentation took place in June, a period when the track is no longer covered in ice. As such, the geometry surveyed corresponds to the underlying concrete surface. It is worth noting that the acquisition conditions were rather challenging: the track was covered with a protective tarp, various wooden structures were present, and the steep vertical sections in the curves significantly degraded the reception of the GNSS signal (see Figure 11).

Prior to data collection, a stereo-preparation field work was conducted, involving the placement of 75 targets arranged in a zigzag pattern along the track. The points are spaced approximately every $\sim$25 m, positioned in relatively open areas along

(a)

(b)

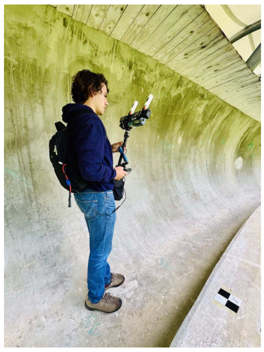

(c)

Figure 11. (a): Image with the track partially open; (b): Image with the track fully covered; (c): Operator performing data acquisition with the SBL system.

the track. Every $\sim$200 m, two targets are placed, one on each side of the track. These targets were surveyed using a geodetic-grade Trimble R12 GNSS receiver. Figure 12 provides an aerial view of the track with the distribution of the targets, while Table 6 gives a synthetic summary of the main characteristics of the acquired data.

Figure 12. Aerial view of Aime-la-Plagne Olympic bobsleigh track and spatial distribution of CPs

The processing pipeline follows the same approach as for the evaluation dataset, with the main difference being that the input data in this case is challenging due to several factors: (i) no loop closure leading to accumulation of errors along the trajectory, (ii) the number of tie points drops off rapidly along axis due to the curves in the track, (iii) although the scene is textured, the number of tie points extracted is relatively low due to the limited contrast in the images. To address this, the images were first enhanced (Rosu et al., 2015) before performing tie point extraction using SIFT (Lowe, 2004), which significantly increased the number of image correspondences, (iv) due to masking, some areas lack GNSS position information associ-

[1] The values are given for positions determined with fixed ambiguities

Stereo-preparation		
N_{CPs}		75
hor. uncertainty [mm]	min.	10
	max.	46
	moy.	18
vert. uncertainty [mm]	min.	13
	max.	88
	moy.	29

(a)

Image Acquisition				
Sequence	S1	S2	S3	S1, S2, S3
$N_{\texttt{Images}}$	5930	5266	5652	17848
Duration	$\sim$ 3h40	$\sim$ 2h40	$\sim$ 2h45	$\sim$ 9h
avg. Interdist. [m]	0.94	1.06	0.86	0.95

(b)

GNSS Acquisition			
GNSS receiver		G1	G2
$N_{Positions}$		6147 / 8924 ($\sim$ 77 %)	8400 / 8924 ($\sim$ 94 %)
Ambiguities Fixed pos.		4223 pos. ($\sim$ 69 %)	4467 pos. ($\sim$ 53 %)
hor. [1] [mm]	min.	20	10
	max.	150	150
	moy.	41	38
vert. [1] [mm]	min.	20	20
	max.	180	170
	moy.	63	61

(c)

Table 6. Main characteristics of the collected data: (a): Stereo-preparation field work; (b): Image acquisition; (C): GNSS positions associated to images.

ated with the images. Note that for the remaining GNSS data collected, only positions with fixed ambiguities are retained for the bundle adjustment compensation.

The initial experiment was planned to include a field work stereo-preparation phase followed by a central acquisition along the track (sequence S1 in Table 6b). Since both parts were successfully completed and some time remained on site, two additional sequences were recorded: sequence S2 on the right of the track and sequence S3 on the left. However, the results are presented for the sequence S1 only as the processing of the three sequences together resulted on a consequent dataset requiring significant resources. The main interest of the two additional sequences concerns mainly the dense reconstruction part, in particular the reconstruction of the edges of the track. Figure 13 shows the results from the acquisition.

To evaluate the performance of our system, we computed the discrepancies between the predicted coordinates of the CPs and their corresponding ground-truth measurement coordinates. Figure 14 illustrates the computed deviations.

Without using any GCPs during the bundle adjustment process, the predicted CPs yields a mean 3D error of 62 mm with a dispersion of ± 24 mm. For sequence S1, out of 5930 images, 3204 have GNSS positions with fixed ambiguities, representing 54% of the sequence.

For this dataset, significantly longer than the evaluation dataset, and to highlight the contribution of the rigid block constraint, a spatial similarity transformation was computed using all GCPs. Two bundle adjustment runs were performed without using any GNSS constraint: (i) without the rigid block constraint and (ii) with the rigid block constraint. Figure 15 presents the residuals on the GCPs for each configuration.

In the absence of GNSS constraints, we observe that introducing the rigid block constraint significantly reduces the drift error.

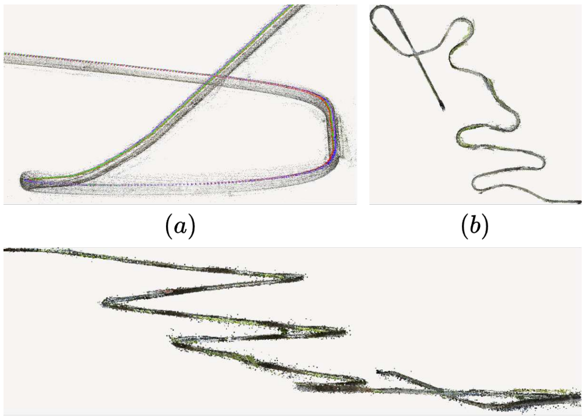

(a) (b) (c)

Figure 13. Results from the acquisition campaign. (a): Overview of the acquisition geometry with a zoomed-in view of the final curve of the track; (b): Top view of tie points; (c): Side view of tie points.

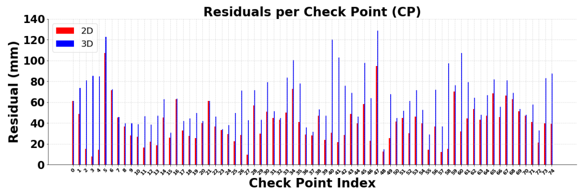

Figure 14. Residuals on CPs

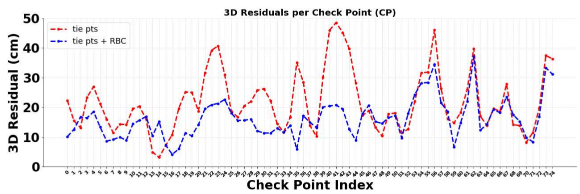

Figure 15. Residuals on GCPs

On this dataset, it results in an improvement by a factor of x1.3. The average error on the GCPs with the rigid block constraint is 16 cm with an uncertainty of ± 7 cm, compared to 22 cm with a ± 10 cm uncertainty when the constraint is not applied. A temporal rigidity constraint was also tested, but it did not yield any significant improvement.

5. Conclusion

This paper focuses on evaluating the performance of a custom built acquisition system composed of two cameras and two GNSS receivers. The system was assembled internally as part of a collaboration with the LadHyX[2] laboratory, which is conducting research to enhance the performance of French athletes within the framework of the Sciences 2024[3] initiative. A key objective of this collaboration is to produce a 3D model of the Olympic bobsleigh track of Aime-la-Plagne in order to perform trajectory simulations on the as-built structure. These simulations aim to identify optimal trajectory that minimize time.

Although the system still has some limitations, most notably in synchronization quality, which currently restricts its use to low

[2] https://www.ladhyx.polytechnique.fr/fr/
[3] https://sciences2024.polytechnique.fr/

dynamic kinematic applications, it has demonstrated promising performance under ideal conditions. With a rigorous calibration protocol, the system achieved an absolute 3D accuracy of $22\,\mathrm{mm}$ and an uncertainty of $\pm\,5\,\mathrm{mm}$ over a linear segment of $\sim 80\,\mathrm{m}$. The system was then deployed for a full acquisition of the bobsleigh track, a challenging environment featuring a singular geometry of nearly $2\,\mathrm{km}$, GNSS signal obstructions, and no possibility of loop closure. Despite these difficulties and without using any GCPs, the system achieved an absolute 3D accuracy of $62\,\mathrm{mm}$ with an uncertainty of $\pm 24\,\mathrm{mm}$.

This experimental validation demonstrates the potential of lightweight, low-cost acquisition systems for photogrammetric applications where high georeferencing accuracy is required. It paves the way for future developments aimed at producing reliable, GCP free acquisition for a wide range of mapping applications.

Acknowledgment

We would like to thank IGN for supporting this work. GEOBSYS company contributed to the sensor integration: Olivier Martin did the mechanical interface design, and Gwennaël Guichard handled the receiver configurations. Philippe Matter assisted with mechanical aspects and the operation of the system using external batteries. We also thank Christophe Clanet and Samy Ben Hamoudi from the LadHyX laboratory for this collaboration, as well as the La Plagne track staff for providing access to the site.

References

Cavegn, S., Haala, N., 2016. Image-based mobile mapping for 3D urban data capture. *Photogrammetric engineering & remote sensing*, 82(12), 925–933.

Chazalet, M., 1991. Piste combinée de Bobsleigh et de luge de La Plagne: métrologie temps réel... appliquée au génie civil. *XYZ*, 19–31.

Elhashash, M., Albanwan, H., Qin, R., 2022. A Review of Mobile Mapping Systems: From Sensors to Applications. *Sensors*, 22(11). https://www.mdpi.com/1424-8220/22/11/4262.

Fraser, C. S., 1997. Digital camera self-calibration. *ISPRS Journal of Photogrammetry and Remote sensing*, 52(4), 149–159.

Huang, W., Jiang, S., Jiang, W., 2021. Camera self-calibration with GNSS constrained bundle adjustment for weakly structured long corridor UAV images. *Remote Sensing*, 13(21), 4222.

IGN, 2024. Comp3d.

James, M. R., Robson, S., 2014. Mitigating systematic error in topographic models derived from UAV and ground-based image networks. *Earth surface processes and landforms*, 39(10), 1413–1420.

Jeong, J., Cho, Y., Shin, Y.-S., Roh, H., Kim, A., 2019. Complex urban dataset with multi-level sensors from highly diverse urban environments. *The International Journal of Robotics Research*, 38(6), 642-657. https://doi.org/10.1177/0278364919843996.

Lowe, D. G., 2004. Distinctive image features from scale-invariant keypoints. *International journal of computer vision*, 60, 91–110.

Maset, E., Rupnik, E., Pierrot-Deseilligny, M., Remondino, F., Fusiello, A. et al., 2021. Exploiting multi-camera constraints within bundle block adjustment: An experimental comparison. *International Archives of the Photogrammetry, Remote Sensing and Spatial Information Sciences*, 43(2-2021), 33–38.

Muller, J.-M., Daakir, M., Pierrot Deseilligny, M., Barcet, F., 2024. Implementation of coded targets for metrology applications in MicMac, a free open-source photogrammetric software. *The International Archives of the Photogrammetry, Remote Sensing and Spatial Information Sciences*, XLVIII-2/W7-2024, 89–96. https://isprs-archives.copernicus.org/articles/XLVIII-2-W7-2024/89/2024/.

Pierrot Deseilligny, M., Cléry, I., 2012. Apero, an open source bundle adjusment software for automatic calibration and orientation of set of images. *The International Archives of the Photogrammetry, Remote Sensing and Spatial Information Sciences*, 38, 269–276.

Pierrot-Deseilligny, M., Jouin, D., Belvaux, J., Maillet, G., Girod, L., Rupnik, E., Muller, J., Daakir, M., Choqueux, G., Deveau, M., 2014. Micmac, apero, pastis and other beverages in a nutshell. *Institut Géographique National*, 14.

Puente, I., González-Jorge, H., Martínez-Sánchez, J., Arias, P., 2013. Review of mobile mapping and surveying technologies. *Measurement*, 46(7), 2127–2145.

Rosu, A.-M., Assenbaum, M., De la Torre, Y., Pierrot-Deseilligny, M., 2015. Coastal Digital Surface Model On Low Contrast Images. *The International Archives of the Photogrammetry, Remote Sensing and Spatial Information Sciences*, XL-3/W3, 307–312. https://isprs-archives.copernicus.org/articles/XL-3-W3/307/2015/.

Rupnik, E., Daakir, M., Pierrot Deseilligny, M., 2017. MicMac–a free, open-source solution for photogrammetry. *Open geospatial data, software and standards*, 2, 1–9.

Septentrio, 2023. mosaic-X5 Reference Guide Applicable to version 4.14.4 of the Firmware. Greenhill Campus, Interleuvenlaan 15i 3001 Leuven, Belgium.

Skaloud, J., 2006. Reliability in direct georeferencing: An overview of the current approaches and possibilities. *EuroSDR workshop EuroCOW on Calibration and Orientation, Castelldefels, Spain*.

Zhou, Y., Rupnik, E., Faure, P.-H., Pierrot-Deseilligny, M., 2018. GNSS-Assisted Integrated Sensor Orientation with Sensor Pre-Calibration for Accurate Corridor Mapping. *Sensors*, 18(9). https://www.mdpi.com/1424-8220/18/9/2783.